JGR Atmospheres

RESEARCH ARTICLE
10.1029/2019JD030378

The Surface Energy Balance at Panda 1 Station, Princess Elizabeth Land: A Typical Katabatic Wind Region in East Antarctica

Minghu Ding[1,2], Diyi Yang[1], Michiel R. van den Broeke[3], Ian Allison[4], Cunde Xiao[2], Dahe Qin[2], and Baojuan Huai[1,5]

[1]State Key Laboratory of Severe Weather, Chinese Academy of Meteorological Sciences, Beijing, China, [2]State Key Laboratory of Cryospheric Science, Northwest Institute of Eco-Environment and Resources, Chinese Academy of Sciences, Lanzhou, China, [3]Institute for Marine and Atmospheric Research, Utrecht University, Utrecht, Netherlands, [4]Antarctic Climate and Ecosystems Cooperative Research Centre, Hobart, Tasmania, Australia, [5]College of Geography and Environment, Shandong Normal University, Jinan, China

Abstract Using automatic weather station and reanalysis data (ERA5) from 2011 at Panda-1 Station, situated in the katabatic region of Princess Elizabeth Land, East Antarctica, the surface energy balance was calculated using a surface temperature iteration method, and the characteristics of each energy component were analyzed. Downward shortwave and longwave radiation were the two primary energy sources during summer days with seasonal means of 346 and 142 W m^{-2}. The turbulent fluxes of sensible and latent heat flux represent smaller heat sources. In the annual mean, reflected shortwave radiation exceeds the upward longwave radiation with a seasonal average values of −287 W m^{-2}. During winter, the shortwave radiation is small, and the main energy input and output terms of the surface energy balance are downward and upward longwave radiation, with seasonal average values of 149 and −159 W m^{-2}, respectively. The combination of high wind speed and a large near-surface humidity gradient during summer resulted in significant frost depositional events. The total surface frost deposition for the whole year was 24 kg m^{-2}, which accounted for 61% of the total accumulation (averaged over 10 years). When a high-pressure ridge blocks cyclones and deflects fronts of low-pressure systems to inland East Antarctica during winter, this has a significant impact on the surface energy balance at Panda 1 automatic weather station, with daily sensible and latent heat fluxes increasing by as much as 25 and 12 W m^{-2}, respectively. These results still contain uncertainties as we only address a single year, when interannual variability may be considerable, and we do not consider drifting snow sublimation.

Key Points:
- Data from Panda 1 AWS and ERA5 reanalysis from 2011 were used to estimate the surface energy balance in the typical katabatic wind zone of East Antarctica
- The influence of two warm and moist air intrusions from the Southern Ocean on the surface energy balance is presented
- Better SEB algorithm scheme in Katabatic areas of Antarctica is validated and promoted

Correspondence to:
M. Ding and H. Baojuan,
dingminghu@foxmail.com;
huaibaojuan@126.com

Citation:
Ding, M., Yang, D., van den Broeke, M., Allison, I., Xiao, C., Qin, D., & Huai, B. (2020). The surface energy balance at Panda 1 Station, Princess Elizabeth Land: A typical katabatic wind region in East Antarctica. *Journal of Geophysical Research: Atmospheres*, *125*, e2019JD030378. https://doi.org/10.1029/2019JD030378

Received 26 JAN 2019
Accepted 19 DEC 2019
Accepted article online 23 DEC 2019

1. Introduction

As one of the world's most important heat sinks, changes in the Antarctic surface energy balance (SEB) have an important impact on the Antarctic and global atmosphere (Braun et al., 2001; Huang, 2008; Randall et al., 1992). Robust estimates of Antarctic SEB are vital for the study of climate change (King et al., 2017; Van As, Van den Broeke, & Roderik, 2005; Van As, Van den Broeke, Reijmer et al., 2005) but also provide ground truthing for satellites and models. Many studies address the Antarctic SEB, but study sites are often located in the Antarctic Peninsula or represent coastal and sea ice without snow cover (e.g., Bian et al., 1991; Bliss et al., 2011; Braun et al., 2001; Heil et al., 1996). Some studies characterized the surface turbulent and radiative fluxes on the inland plateau and in the katabatic wind region (e.g., Kuhn et al., 1977; Van den Broeke, Van As, Reijmer, et al., 2005; Argentini et al., 2014), but only a few systematic studies on complete SEB have been carried out in this region (Carroll, 1982; Van den Broeke, Reijmer, van As, et al., 2005; King et al., 2006; Town & Walden, 2009). Because these areas represent a large fraction of the vast area of Antarctica and still show considerable spatial climate variability, more information is needed on how the ice/snow interacts with the atmosphere in East Antarctica.

Princess Elizabeth Land appears as a typical East Antarctic katabatic wind region; the area has a very large topographic backdrop, high wind speeds, and a very constant wind direction (Chen et al., 2007; Ding et al., 2011; Ding et al., 2017). Due to continuous erosion and densification, the surface snow can be characterized as a "glazed surface" (Ding et al., 2015; Scambos et al., 2012). The SEB of the katabatic wind region is

distinct from that of the coastal region, which is characterized by the abrupt transition from grounded (sloped) to floating (flat) ice, and is bordered by the sea ice or the ocean. Due to the lower cloud cover in the katabatic wind zone in combination with an efficient turbulent heating of the surface, the longwave radiative loss of the snow surface to the atmosphere is usually higher than in the coastal region (Van den Broeke et al., 2006). This dominates the shortwave effect of less clouds, resulting in a net radiative heat loss of the surface, which is unique to the large ice sheets. Van den Broeke, et al. (2004a) showed that in Dronning Maud Land (DML), the katabatic wind zone experienced more net radiative heat loss than the coast and interior plateau based on data from four automatic weather stations (AWSs) at different elevations. Fu et al. (2015) confirmed that the annual mean net radiation in the katabatic wind zone of Princess Elizabeth Land was more negative than the dome areas such as Vostok and Dome C further east.

Unfortunately, eddy correlation systems, which are the most accurate experimental approach to measure turbulent heat fluxes, are difficult to operate in polar regions, especially in strong winds areas, for the low temperatures and frequent drifting snow disturb the measurements of the ultrasound sensor (Vignon, Genthon, Barral, Amory, et al., 2017). Therefore, turbulent heat fluxes are usually estimated using the bulk aerodynamic method (King et al., 1996; Van den Broeke, Van As, Reijmer, et al., 2005; Van den Broeke, Reijmer, van As, et al., 2005; Rinke et al., 2012). These studies found that, especially during winter, the strong longwave radiative heat loss is compensated by downward turbulent sensible heat transport, which is enabled by the high katabatic wind speeds (Van den Broeke, et al., 2004b; Van den Broeke et al., 2005). Wind-driven processes thus not only play a role in shaping the surface morphology and affect the snow surface roughness but also transport significant amounts of sensible and latent heat, even under drifting snow conditions (Bintanja, 2001; Bintanja & Reijmer, 2001; Frezzotti et al., 2002; Eisen et al., 2009; Ding et al., 2017). For instance, over the ablation zone of Taylor Glacier, the sublimation rate could reach up to 0.4 m a^{-1} under the influence of strong katabatic winds (Bliss et al., 2011). Over the dark blue ice in Antarctica near the Swedish Svea station (albedo ~0.55), Bintanja and Van den Broeke (1995) also observed strong sublimation as well as a negative sensible heat in summer (convection) in response to enhanced solar radiation absorption, while the adjacent snow surface area had weak sublimation and a positive sensible heat flux.

The surface mass and energy balance of the Antarctic ice sheet is also sensitive to small changes in meteorology and topography (Huybrechts, 1990; Marsiat & Bamber, 1997; Gallée et al., 2001; Sun et al., 2018). Extratropical cyclones have a great impact on the Antarctic SEB, particularly when they are land-tracking (Andersen et al., 2013; Rinke et al., 2017; Woods et al., 2013; Xie et al., 2002). Polar cyclones in this sector of East Antarctica develop mostly in the southern Indian Ocean to the northwest of Prydz Bay, with more cyclones in winter than in summer (Simmonds & Keay, 2000; Qin et al., 2017). Most cyclones weaken significantly after entering the region of Prydz Bay and dissipate before reaching the interior ice sheet. As a result, a large fraction of cyclones does not impact the SEB at Panda-1 Station (Qin et al., 2017). When mild and humid air does reach interior Antarctica, significant fluctuations in local humidity and temperature have been observed (Genthon et al., 2013; Vignon et al., 2018). Braun et al. (2001) studied the effects of large-scale atmospheric circulation variability on surface melting in the Antarctic Peninsula and found that the SEB and melt rate were strongly related to large-scale atmospheric conditions. Based on Lagrangian moisture source diagnostics, Wang et al. (2013) found that the moisture sources for precipitation over Dome Argus (Dome A) were mainly situated in the midlatitude south Indian Ocean, confirming the influence of midlatitude moisture sources on the climate of interior East Antarctic.

In summary, to enhance our understanding of Antarctic climate and further improve climate/numerical weather prediction models over Antarctica and specifically over Princess Elizabeth Land, it is necessary to understand the SEB process in its katabatic zone and the effects of synoptic weather systems. This study uses AWS measurements to quantify the SEB at Panda-1 site, situated in the katabatic wind zone along the Chinese National Antarctic Research Expedition (CHINARE) traverse, from Zhongshan Station to Dome A. We estimate the SEB uncertainty using sensitivity tests, and we compare our results with results from other Antarctic sites. The effects of synoptic weather systems on the inland climate and SEB during two maritime air intrusions are discussed. The paper is structured as follows. Section 2 introduces the Panda-1 Station and SEB model. Meteorological conditions and the impacts of two warm, moisture intrusions are described in section 3. Section 4 systematically analyses (annual/daily) SEB component variations and these are compared to the SEB at other Antarctic sites in section 5, which also includes the model evaluation. Section 6 presents conclusions.

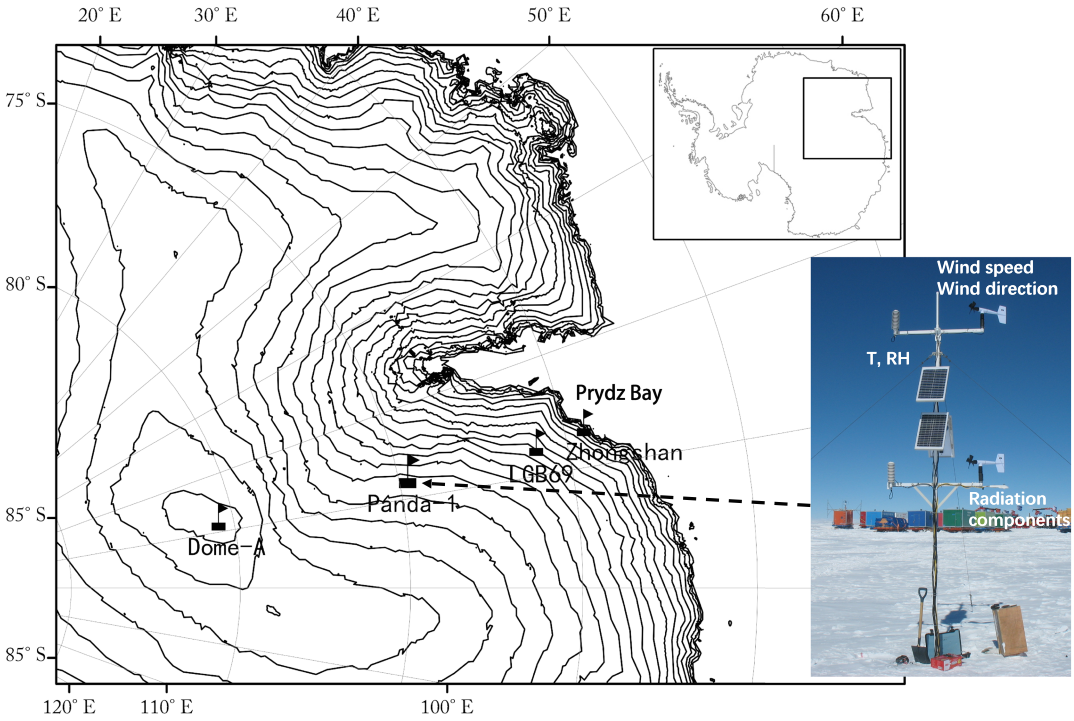

Figure 1. Topography and location of Panda-1 AWS in the CHINARE traverse route (the black solid lines are for the contour interval of 200 m).

2. Methods

2.1. Location and Sensor Specifications

The Panda-1 AWS (74°39′S, 77°E; 2,737 m above sea level) is situated in the katabatic wind region of Princess Elizabeth Land, ~580 km inland from coastal Zhongshan Station, East Antarctica (Figure 1). The estimated large-scale surface slope is approximately 5 m km^{-1}, and the surface is homogeneous (Ding et al., 2015). Panda-1 AWS sensor specifications are shown in Table 1. Double-level measurements of wind, naturally ventilated relative humidity (RH), and air temperature (T) were performed at heights of approximately 2 and 8 m. The air pressure sensor was placed in the electronics enclosure, and the snow temperature was measured at initial depths of 0.1 and 0.4 m. In addition, the four radiation components were measured by a single radiometer. Sampling of all the sensors was performed at 10-min intervals except for the pressure sensor (1 hr). Subsequently, the Campbell CR5000 data logger stored 1-hr average values.

2.2. Data Processing

The selected observation period for this study was from 1 January to 31 December 2011. In polar regions, strong wind and low temperature usually have a significant impact on the sensors, as ice can accrete on the wind speed/direction sensor in winter and invalidate the measurements. As a result, a total of 4,141 wind speed values were missing from May to October 2011, representing 47.3% of the total wind speed data. There were no available wind speed data at adjacent stations during the icing episodes. Vignon et al. (2019) showed that ERA5 better reproduces wind speed vertical profiles at coastal Antarctic sites than ERA-Interim, and we repeated the wind speed evaluation for Panda-1 Station based on the complete data sets in 2016, with a (data) resolution of 0.25°. The yearly average bias and RMSE between ERA5 10-m wind speed and observed 2-m measured wind speed were −0.4 and 1.5 m/s (r = 0.86), with values of −0.6, 1.7 m/s in summer (December-January-February) and −0.6, 1.7 m/s in winter (June-July-August), respectively. We conclude that ERA5 10-m wind speed provides a reasonable representation of wind speed at Panda-1 AWS, and we use it to fill the wind speed data gaps by linearly interpolating the nearest grid points. Reflected shortwave radiation was missing from 1 to 23 January. We filled this missing data with solar radiation measurements during the missing period and average albedo over the remaining period in January. Other sensors

Table 1
AWS Sensor Specifications

Sensor	Type	Range	Accuracy
Air temperature	Vaisala HMP155	-80 to +60 °C	±(0.176-0.0028 × temperature) °C
Relative humidity	Vaisala HMP155	0 to 100%	±(1.2 + 0.012 × reading) %RH
Air pressure	CSI CS106	500 to 1,100 hPa	±1.5 hPa(-40 to +60 °C)
Wind speed	XFY3—1	0 to 100 m/s	±0.5 m/s or ±0.5%
Wind direction	XFY3—1	0 to 360°	±5°
Pyranometer	Kipp&Zonen CNR4	305 to 2,800 nm	EADT ±10%
Pyrgeometer	Kipp&Zonen CNR4	4,500 to 42,000 nm	EADT ±10%

EADT = estimated accuracy of daily total.

performed well, and the data integrity was good. No snow surface height records were available, so the meteorological parameters were not corrected for height change. Instead, we estimated the sensitivity to snow surface height variations in the SEB components using the stake record (see section 5.2).

2.3. Energy Balance Model

We applied the surface energy balance equation to hourly average AWS data:

$$(1-\alpha)SR_{\downarrow} + LR_{\uparrow} + LR_{\downarrow} + SHF + LHF + G = Q_M \quad (1)$$

All terms are defined as positive when the energy flux is directed toward the snow surface. $SR_{\downarrow}$ and α are the downward solar radiation flux and snow surface albedo, respectively, and $LR_{\uparrow}$ and $LR_{\downarrow}$ are upward and downward longwave radiation fluxes, respectively. SHF and LHF are the sensible and latent turbulent heat fluxes, respectively. G is the surface value of the subsurface conductive heat flux in the snow. Q_M is the residual energy that is used for melting of surface snow, which is zero if the surface temperature is below 273.15 K.

The relatively poor cosine response of the used type of pyranometer has the potential to cause a significant error in $SR_{\downarrow}$ when the zenith angle is large. To largely eliminate errors in $SR_{\downarrow}$ that are associated with a poor cosine response, we used an "accumulated" albedo method (Van den Broeke, et al., 2004a) to calculate the net shortwave radiation based on $SR_{\uparrow}$ (upward shortwave radiation), which is much less sensitive to cosine error uncertainties than $SR_{\downarrow}$.

$$SR_{net} = -SR_{\uparrow}(1+\alpha)/\alpha \cong -SR_{\uparrow}(1+\alpha_{acc})/\alpha_{acc} \quad (2)$$

$$\alpha_{acc} = \sum_{24h} |SR_{\uparrow}| / \sum_{24h} SR_{\downarrow} \quad (3)$$

where α_{acc} is the "accumulated" albedo, which is the ratio of accumulated $|SR_{\uparrow}|$ and $SR_{\downarrow}$ over a time window of 24 hr centered on the observation time. This method does only partly address riming problems. Intrusions of warm and moist air masses can deposit rime on the upward looking dome of the radiation sensor and change the transmittance of the glass dome (Van den Broeke et al., 2003; Yang et al., 2018). For example, transmittance is reduced if there is a thick ice coating on the dome, while the transmittance is overestimated at low sun angles with a thin ice coating. Because it does not cool to space, the downward directed glass dome is less susceptible to riming, but α_{acc} will be affected if riming persists over the daytime period.

The bulk aerodynamic flux equations with stability corrections based on Monin-Obukhov similarity theory were used to calculate the turbulent heat fluxes. This method generally shows an acceptable correlation with eddy-covariance measurements in Antarctica (Van den Broeke, Van As, Reijmer, et al., 2005). However, MO theory requires a stationary state for wind, temperature, and humidity fields (Vignon, Genthon, Barral, Amory, et al., 2017). In order to address this, we removed 4.4% of the data which were nonstationary condition and with whose 1-hr difference with the previous sample exceeded 1.8 °C, 2.7 m/s. The expressions used to calculate the sensible and latent heat fluxes are as follows:

$$H = \rho C_p u_* \theta_* \tag{4}$$

$$LE = \rho L_v u_* q_* \tag{5}$$

$$u_* = \frac{ku}{ln\left(\frac{z}{z_{om}}\right) - \psi_M\left(\frac{z}{L}\right) + \psi_M\left(\frac{z_{om}}{L}\right)} \tag{6}$$

$$\theta_* = \frac{k(\theta - \theta_s)}{ln\left(\frac{z}{z_{ot}}\right) - \psi_H\left(\frac{z}{L}\right) + \psi_H\left(\frac{z_{ot}}{L}\right)} \tag{7}$$

$$q_* = \frac{k(q - q_s)}{ln\left(\frac{z}{z_{oq}}\right) - \psi_E\left(\frac{z}{L}\right) + \psi_E\left(\frac{z_{oq}}{L}\right)} \tag{8}$$

Here u_*, θ_*, and q_* are the associated turbulent scales. k is the Karman constant ($k = 0.4$); ρ and P are the air density ($\rho = \frac{PM}{RT}$) and air pressure at the site level; M and R are the molar mass of air and the gas constant, respectively; C_p is the specific heat capacity for air (1,005 $J \cdot kg^{-1} \cdot k^{-1}$); L_v is the latent heat of snow sublimation (2.834 $MJ \cdot kg^{-1} \cdot k^{-1}$); u, θ, and q are the wind speed, potential temperature, and specific humidity at AWS measurement level (z); and subscript "s" denotes surface values. The potential temperature, air, and surface specific humidity (q and q_s) equations are as follows (Bolton, 1980):

$$\theta = T\left(\frac{P_0}{P}\right)^{\frac{R}{C_p}} \tag{9}$$

$$q = \frac{\epsilon}{P} \cdot RH \cdot 611.2 \exp\left(\frac{17.67(T - 273.15)}{T - 29.65}\right) \tag{10}$$

$$q_s = \frac{\epsilon}{P} \cdot RH_s \cdot 610.78 \exp\left(\frac{21.8745584(T - 276.16)}{T - 7.66}\right) \tag{11}$$

RH and RH_s are the air and surface relative humidity. We assumed a saturated snow surface ($RH_s = 100\%$), while ϵ is the ratio of molar masses between water and air ($\epsilon = 0.622$). ψ_M, ψ_H, and ψ_E are the nondimensional stability correction functions for momentum, heat, and moisture, respectively, which depend on $\frac{Z}{L}$, where $L = \frac{u_*^2 \theta}{gk(\theta_* + 0.62\theta q_*)}$ is the Monin-Obukhov length.

For stable conditions ($\frac{Z}{L} > 0$), we use the expressions due to Beljaars and Holtslag (1991) with a = 1, b = $\frac{2}{3}$, c = 5, d = 0.35:

$$\psi_M\left(\frac{z}{L}\right) = -\left(a\frac{z}{L} + b\left(\frac{z}{L} - \frac{c}{d}\right)\exp\left(-d\frac{z}{L}\right) + \frac{bc}{d}\right) \tag{12}$$

$$\psi_H\left(\frac{z}{L}\right) = \psi_E\left(\frac{z}{L}\right) = -\left(\left(1 + \frac{2az}{3L}\right)^{1.5} + b\left(\frac{z}{L} - \frac{c}{d}\right)\exp\left(-d\frac{z}{L}\right) + \frac{bc}{d} - 1\right) \tag{13}$$

For unstable conditions ($\frac{Z}{L} < 0$), Dyer's expression was used (Dyer, 1974):

$$\psi_M\left(\frac{z}{L}\right) = 2\ln\left(\frac{1 + x}{2}\right) + \left(\frac{1 + x^2}{2}\right) - 2\arctan x + \frac{\pi}{2} \tag{14}$$

$$\psi_H\left(\frac{z}{L}\right) = \psi_E\left(\frac{z}{L}\right) = 2\ln\left(\frac{1 + x^2}{2}\right) \tag{15}$$

$$x = \left(1-16\frac{z}{L}\right)^{\frac{1}{4}} \tag{16}$$

z_{om}, z_{oq}, and z_{ot} are defined as the surface roughness lengths for momentum, specific humidity, and temperature. Different surface states and atmospheric conditions correspond to different surface roughness length values. According to the expression of the surface layer wind speed profile, where ψ_M is neglected as a first guess:

$$u \cong \frac{u_*}{k}\left(\ln\left(\frac{z}{z_{om}}\right)-\psi_M\right) \tag{17}$$

we can get estimate an initial value for z_{om} based on two measurement levels. Next, based on Reynolds number ($Re_* = u_* z_0 \upsilon^{-1}$), as proposed by Andreas (1987), we obtained z_{oq} and z_{ot}, where υ is the kinematic viscosity of air. After several iterations the Monin-Obukhov length (L) and the roughness lengths converged for all data.

The subsurface heat flux G consists of the penetration of shortwave radiation flux and conductive heat flux. The penetration of shortwave radiation flux $S_i(z) = (1-\alpha)\mathrm{SR}_{\downarrow} \cdot (1-\mathrm{a})e^{-bz}$ decreases exponentially as the depth z increases which a and b set to 0.8 and 2.5 in this paper (Bintanja & Van den Broeke, 1995). The conductive heat flux $G_c = -K_s\frac{\delta T}{\delta z}$ can be estimated using the effective thermal conductivity K_s, the temperature gradient of the subsurface layer $\left(\frac{\delta T}{\delta z}\right)$ which has been evaluated between −0.1 m and the surface. We obtained K_s using an empirical parameterization (Sturm et al., 1997) whose original density data came from China's 29th Antarctic Expedition.

$$K_s = 0.138-1.01\rho_s + 3.233{\rho_s}^2 \quad \{0.156 \le \rho_s \le 0.6\} \tag{18}$$

ρ_s is the density of the surface snow layer. Under the low accumulation conditions here, we assumed the snow density constant ($\rho_s = 0.381$ g cm^{-3}).

The SEB affects and depends on the surface temperature (Bliss et al., 2011). We used an iteration method to achieve closure of the SEB (Bliss et al., 2011; Fujita, 2000); the T_s thus obtained was compared to that observed from $\mathrm{LR}_{\uparrow}$.

3. Meteorological Conditions at Panda Station in 2011

3.1. Surface Meteorological Conditions

Figure 2 shows the daily mean 2 m and surface values of wind speed (zero at the surface), temperature, and water vapor pressure. The differences of temperature and vapor pressure between the two levels are also included. This location in Princess Elizabeth Land appears to be dominated by katabatic winds, with an annual average 2-m wind speed of 10.5 m s^{-1} (Table 2) and a maximum hourly average wind speed of over 20 m s^{-1}. Determined by the net effects of katabatic (downslope) forcing, the Coriolis force, and friction, the dominant wind direction at Panda-1 Station was easterly. Both air temperature and water vapor pressure peaked in summer and reached minima in winter. The surface-to-air temperature and water vapor pressure gradients have a decisive effect on the magnitude and direction of SHF and LHF. The average temperature and vapor pressure at 2 m and the surface in 2011 were −36.3 °C and 27.7 Pa, −37.5 °C, and 20.3 Pa, respectively. Melting does not occur at Panda-1 site since the surface temperature remains significantly negative year-round. The water vapor pressure, whose vertical gradient depends on the gradients of relative humidity (saturating during strong blowing event) and on the gradients of temperature, was greater at 2 m than at the snow surface throughout the year. When drifting/blowing snow occurred, the saturated near-surface air layer will be thicker (Bintanja, 2001) and the gradients of water vapor pressure near the surface reduced. The 2-m air temperature on average was

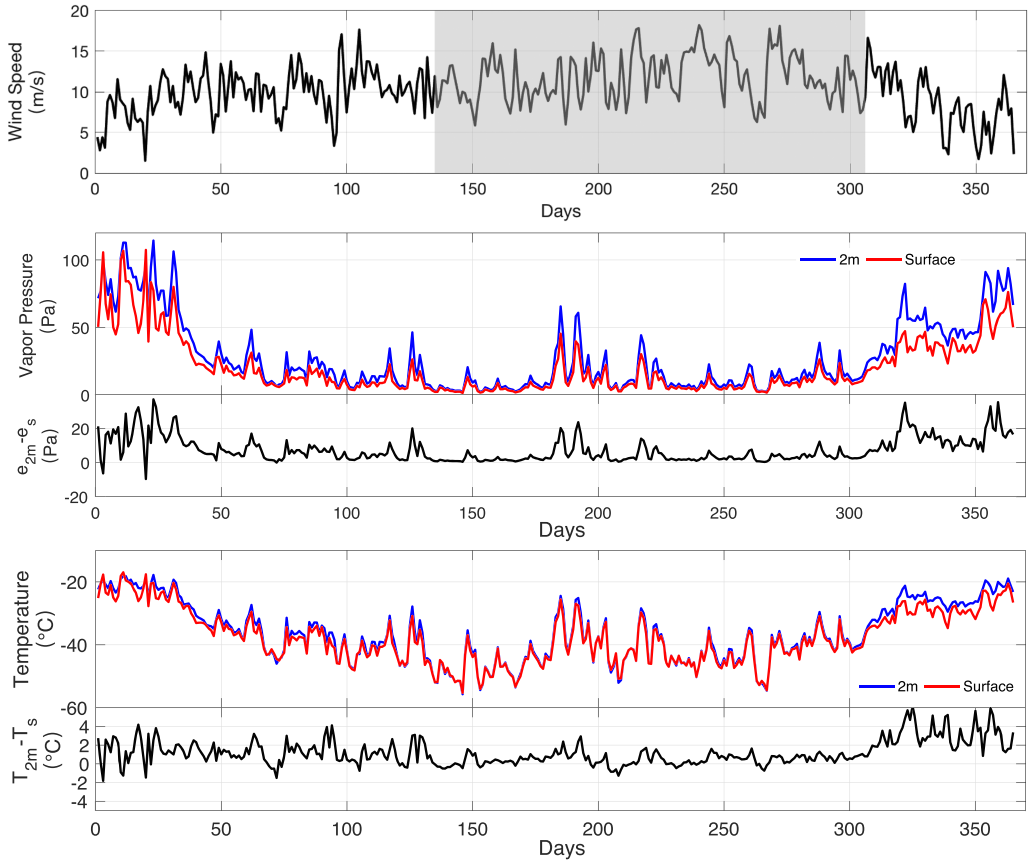

Figure 2. Daily mean values of (a) wind speed (gray zone: reanalyzed data); (b) vapor pressure at the height of 2 m (e_{2m}), snow surface vapor pressure (e_s), and their difference ($e_{2m} - e_s$); and (c) air temperature at the height of 2 m (T_{2m}), snow surface temperature (T_s), and their difference ($T_{2m} - T_s$).

0.5 °C higher than the snow surface temperature due to the persistently negative net longwave radiation.

3.2. Synoptic Weather Systems

Each year, several cyclones stagnate or develop in Prydz Bay (Xie et al., 2002). When the frontal zone moves inland from Prydz Bay in winter, it will bring relatively warm, moist ocean air masses to the ice sheet interior

Table 2
Monthly Average Values of Near-Surface Climate and SEB Components

	T_{2m} (°C)	T_s (°C)	$T_{10\ cm\ depth}$ (°C)	Wind speed (m s^{-1})	e_{2m} (Pa)	e_s (Pa)	$SR_\downarrow$ (W m^{-2})	$SR_\uparrow$ (W m^{-2})	$LR_\downarrow$ (W m^{-2})	$LR_\uparrow$ (W m^{-2})	Conductive heat flux (W m^{-2})	Shortwave radiation penetration (W m^{-2})
Jan	−21.1	−22.5	−21.9	7.9	84.4	67.7	333.2	286.1	167.4	223.0	1.8	−7.3
Feb	−31.3	−32.5	−30.0	10.3	34.0	25.7	256.7	207.6	124.6	187.6	8.7	−7.6
Mar	−37.0	−38.1	−37.2	10.1	20.1	13.7	109.5	83.5	132.2	169.8	3.1	−4.0
Apr	−40.2	−41.5	−40.6	10.8	13.4	8.8	19.1	15.4	139.2	161.5	3.9	−0.6
May	−44.7	−45.2	−44.6	10.2	10.1	6.6	0.0	0.0	138.4	152.7	7.1	0.0
Jun	−46.9	−47.3	−47.4	11.0	6.1	4.4	0.0	0.0	139.3	146.5	−1.3	0.0
Jul	−38.2	−38.7	−39.8	11.2	21.4	14.5	0.0	0.0	163.0	171.1	−5.7	0.0
Aug	−41.9	−42.3	−42.4	13.8	12.7	8.9	4.6	4.0	145.8	159.4	1.4	−0.1
Sep	−43.5	−44.1	−44.0	12.5	10.1	7.0	71.8	51.0	114.8	152.2	0.8	−3.2
Oct	−38.8	−39.5	−40.4	11.6	15.4	11.4	201.7	152.1	112.6	164.7	−6.4	−7.7
Nov	−28.0	−31.0	−33.5	10.5	44.3	30.2	360.8	289.5	121.7	197.2	−14.9	−11.1
Dec	−24.5	−27.6	−27.5	6.4	60.4	45.0	448.5	367.2	134.0	211.3	−4.1	−12.7
Average	−36.3	−37.5	−37.4	10.5	27.7	20.3	150.5	121.4	136.1	174.7	−0.5	−4.5

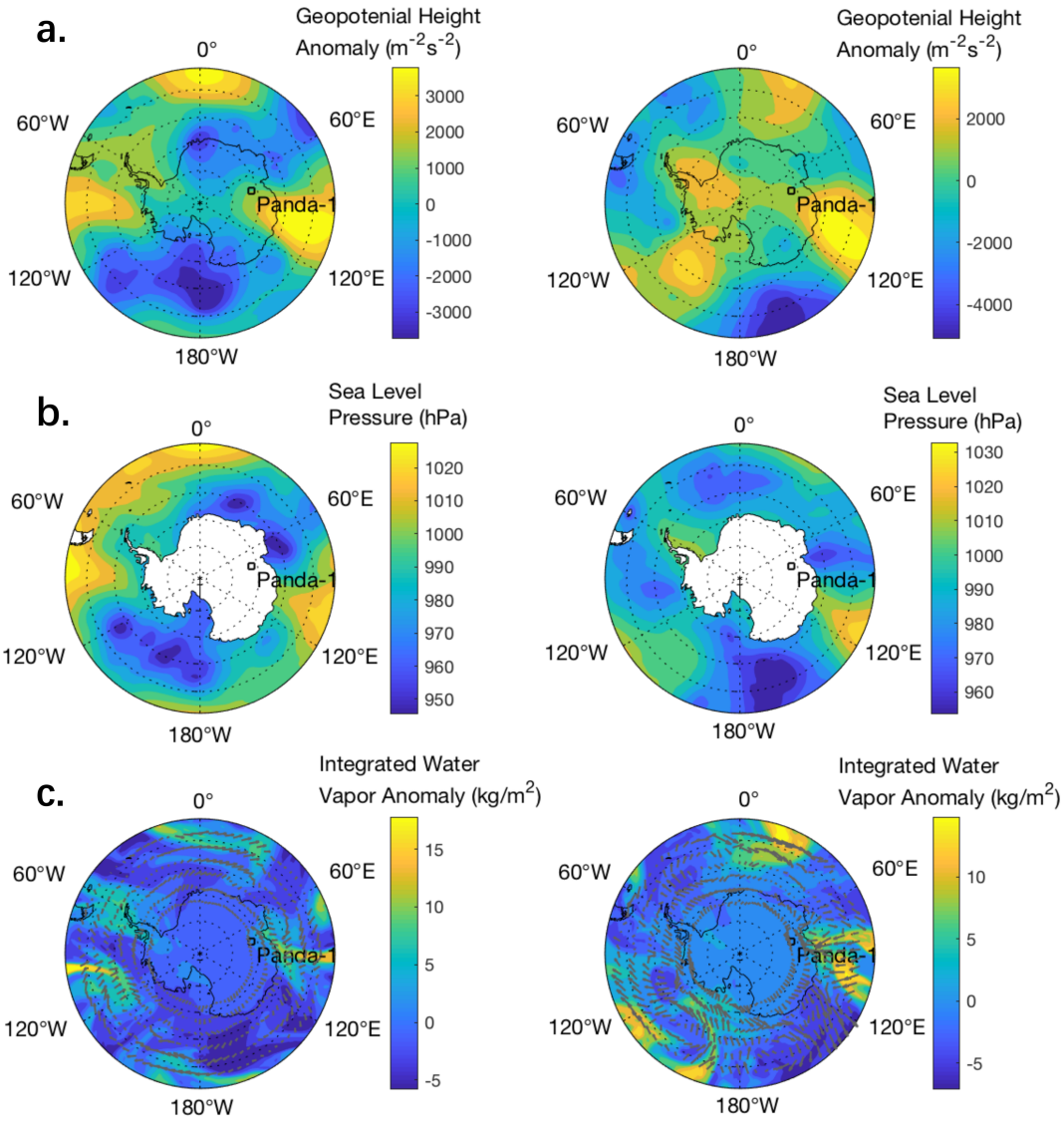

Figure 3. (a) Anomaly of the monthly mean 500-hPa geopotential height with respect to the 1979–2018 mean (July), (b) mean sea level pressure, and (c) integrated water vapor anomaly with respect to the 1979–2018 mean (July) and 850-hPa wind vectors from ERA5 during (left) 3 July 2011 and (right) 9 July 2011.

(Qin et al., 2017). As Figure 2 shows, the Panda-1 AWS registered two such events in early July. Temperature and water vapor pressure rose nearly 70 Pa and 20°C in four days, indicative of maritime air intrusions to Princess Elizabeth Land. Air pressure at the study site (not shown) showed no such changes, suggesting that no direct cyclone intrusion occurred. The average 500-hPa geopotential height anomaly (relative to the 1979–2018 July mean) from ERA5 before these two events strong positive anomalies (Figure 3). The southern section of the Indian Ocean subtropical high is usually flat in the geopotential height field, and cyclones move eastward along its southern edge and eventually dissipate along the coast or over the ocean surface. However, the Indian Ocean subtropical high was obviously extended southward near 100°E on 3 July, which shaped a high-pressure ridge that deeply intruded the inland area. The sea level pressure field showed that a deep low-pressure system was blocked from moving eastward and thus stagnated near Prydz Bay. These synoptic conditions were favorable for the large-scale meridional inland advection of warm, moist air masses (Bozkurt et al., 2018). The blocking situation and northerly wind at the front of the cyclone fed the low-level poleward flow of heat and moisture to Panda-1 AWS, resulting in peak water vapor pressure and temperature on 4 July. On 9 July, similar conditions persisted, although the geopotential height anomaly field and cyclone were slightly weaker. As was shown previously for Dome C (Genthon et al., 2013; Vignon, Hourdin, Genthon, et al., 2017) and Kohnen Base (Van As, Van den Broeke, & Roderik, 2005), this

confirms that the atmospheric boundary layer structure at inland sites can be strongly affected by weather systems, even when the core of these systems does not penetrate far inland.

4. Surface Energy Balance Results

4.1. Radiation and Albedo

The intensity of solar radiation mainly depends on latitude and season, atmospheric transparency, terrain, and solar elevation angle (Iqbal, 1983; Kumar et al., 1997; Liston et al., 1999). The Antarctic atmosphere is clean and has a high transmittance for shortwave radiation, while the topography of Panda-1 Station is flat, which results in less terrain scattering radiation. The summer and annual mean values of downward solar radiation at our site are 346 and 151 W m^{-2}, representing the major input terms to the SEB. Reflected shortwave radiation is primarily determined by the snow surface albedo. The fresh snow surface albedo can be as high as 0.9 and strongly limits shortwave absorption. After metamorphism and sedimentation, the surface albedo can decrease to approximately 0.6 from March to April and from September to October. As shown in Figure 4a and Table 1, the annual mean value of the albedo was 0.81. The sudden, upward albedo changes result from new snow deposited at the AWS site (Bian et al., 1991).

As the primary heat loss component, upward longwave radiation mostly depends on surface temperature. The snow surface temperature at the study site was generally below −20 °C, with an annual average upward longwave radiation of 175 W m^{-2}. According to Kirchhoff's law, the absorptivity of a material is equal to its emissivity at the same wavelength and at thermodynamical equilibrium (Berdahl & Fromberg, 1981). The downward longwave radiative flux depends on the integrated amount of water vapor above the location and on cloudiness, as well as atmospheric temperature (Gallée & Gorodetskaya, 2010; Gubler et al., 2012). The daily average value of downward longwave radiation peaked at 136 W m^{-2}. Peak longwave radiation loss mostly occurred in summer, when the surface is heated by absorption of solar radiation, with an average loss of up to −77 W m^{-2}. In winter, downward and upward longwave radiation are nearly in equilibrium, dominating the SEB, similar to what was found at Dome C (Argentini et al., 2014; Vignon et al., 2018). However, there was significant longwave heat loss (~40 W m^{-2}) existed in Van den Broeke et al. (2005) in the katabatic wind zone DML, compensated by SHF. This may be led by more cloud cover at Panda-1, limiting longwave heat loss.

During the two maritime air mass intrusions, a rapid increase was found in both longwave radiation components (60 W m^{-2}) due to the warming of the atmosphere and subsequently the surface (Figure 4b), reaching a peak around 4 July. Only three days later, values were back to normal.

4.2. Sensible and Latent Heat Fluxes

Figure 2 shows that during summer, both SHF and LHF were greater than during the other seasons (Figures 6 and 8). SHF was positive for most of the year with a daily average of 12 W m^{-2}. This is consistent with the results in Figure 2c that a persistent temperature gradient existed during the study period, which made the snow surface receive heat from the atmosphere. In summer, average SHF reached 11 W m^{-2} while it dropped to 9 W m^{-2} in winter because of the smaller temperature difference between 2 m and the snow surface. Diurnal variability is discussed in section 4.5. LHF was smaller than SHF but also positive most of the time, with a yearly average of 2 W m^{-2}, indicating the atmosphere released heat to the snow surface during frequent riming events. During the winter, the low air temperature limits the absolute water vapor content and gradients, and weakens LHF. Drifting snow will thicken the saturated layer of the near-surface, which reduces the vertical humidity gradient (Mastrantonio et al., 1999). Multiple peaks in vapor pressure in winter slightly increases the average LHF compared to the annual average.

SHF and LHF are sensitive to local heat and moisture variations (Sun et al., 2012; Sun et al., 2018). During maritime air intrusions, increased temperature and humidity combined with a strong wind increased the fluxes during early July (Figure 2): LHF shows a peak hourly value of 18 W m^{-2} around 4 July (Figure 5b). SHF lagged LHF by about one day and increased to more than 40 W m^{-2} around 5 July. A similar lag occurred at 10 July (not shown). This phenomenon may result from intense longwave radiation loss which made the snow surface temperature drop faster and enlarged the temperature gradient

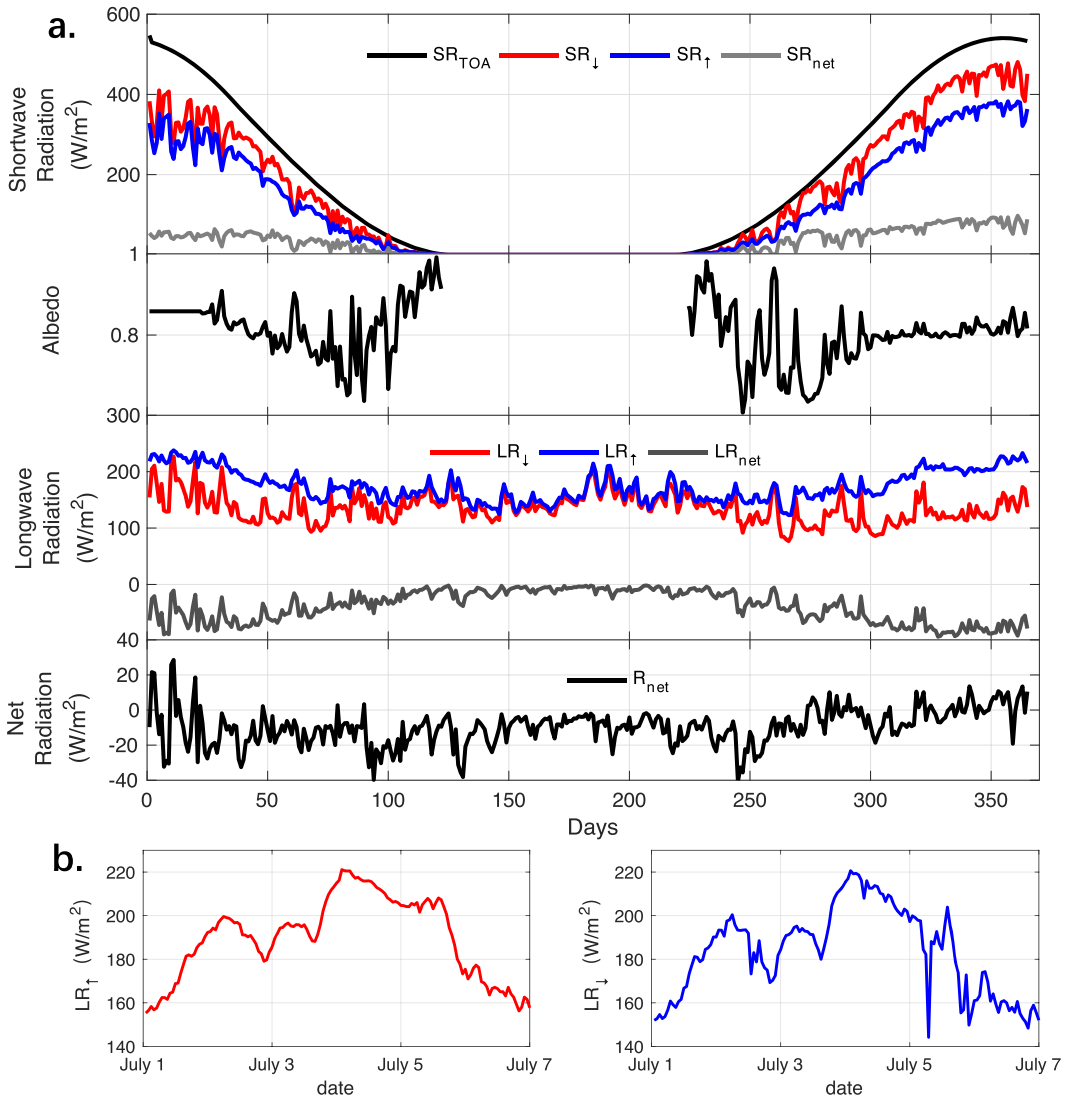

Figure 4. (a) Daily mean values of incident and reflected shortwave radiation, downward and upward longwave radiation, albedo, and net radiation. (b) Hourly means of $LR_{\uparrow}$ and $LR_{\downarrow}$ during one intrusion event in July 2011.

toward the surface. Under cyclonic influence in July, the monthly mean values of LHF increased and reached 4 W m^{-2} (see Table 3).

4.3. Subsurface Heat Flux

The effective thermal conductivity of dry snow mainly depends on its density (Lei et al., 2010). It can vary from less than 0.2 W · K^{-1} · m^{-1} for fine-grained new snow to more than 0.5 W · K^{-1} · m^{-1} for wet or refrozen snow (Lei et al., 2010; Sturm et al., 2002). Thermal conductivity is also expected to vary with depth owing to the sharp gradients of snow density near the surface (Brun et al., 2012). Previously, we deduced from snow surface temperature measurements (propagation and dampening of the temperature wave; Lei et al., 2014) that the effective thermal conductivity at Panda Station at 10-cm depth is 0.22 W · K^{-1} · m^{-1} while the value at 40-cm depth is 0.33 W · K^{-1} · m^{-1}. Figure 6a indicates that the annual amplitude of snow temperature was approximately 5 °C less than the surface snow temperature. The annual average G was only −0.5 W m^{-2}, indicating that during 2011 some energy was transferred from the surface to the snow layer. This mostly occurred in November when

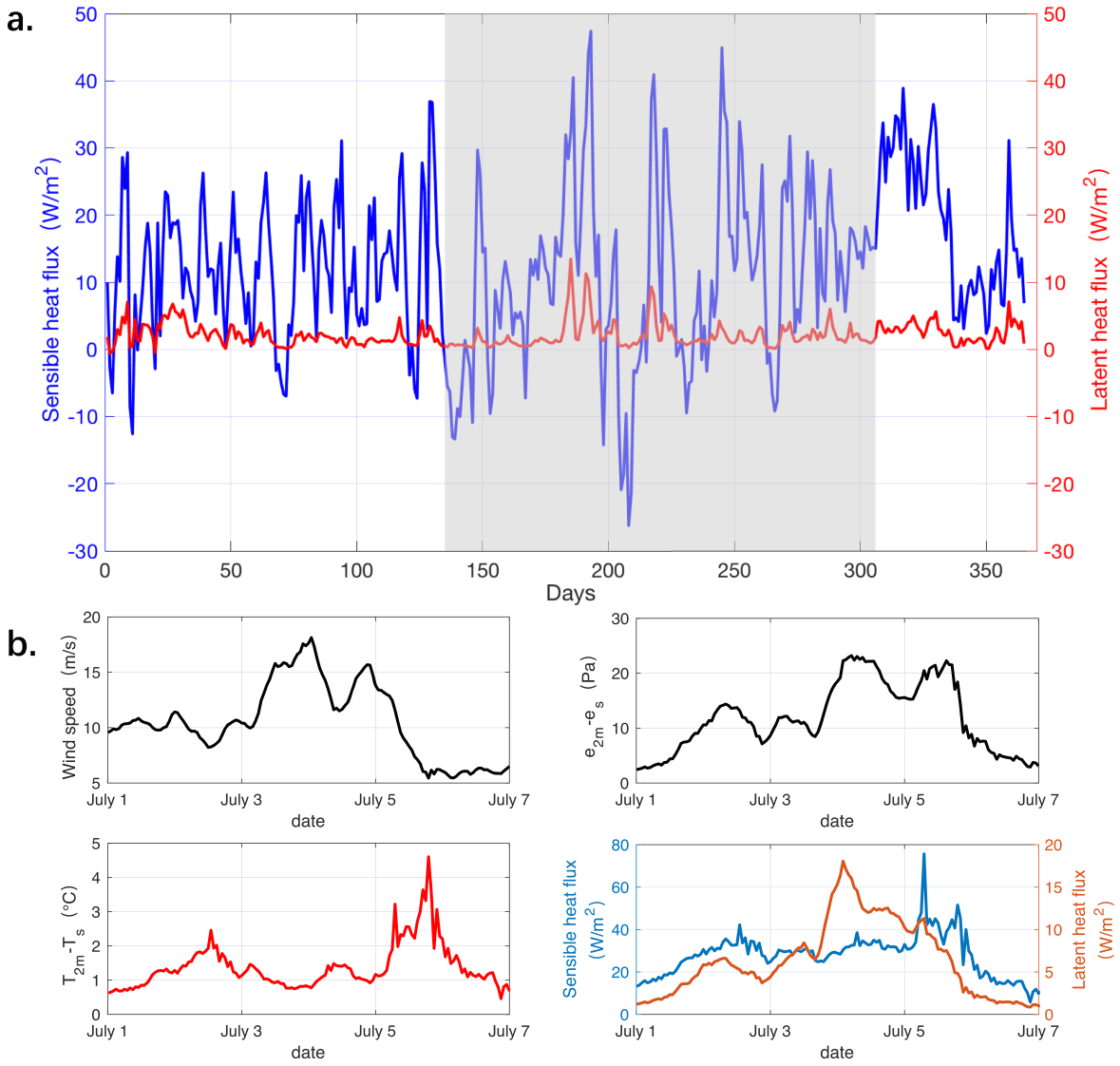

Figure 5. (a) Daily mean values of sensible and latent heat (gray zone: results calculated from reanalyzed wind data). (b) Hourly means of wind speed, $e_{2m} - e_s$, $T_{2m} - T_s$, and sensible and latent heat flux during one intrusion event in July 2011.

solar radiation began to increase significantly, enhancing the upward temperature gradient resulting in a monthly average conductive heat flux of −15 W m^{-2}. Shortwave radiation penetration largely followed net shortwave radiation, and its annual mean value was −5 W m^{-2}.

During intrusions of warm and moist air masses, the temperature of the snow surface increased rapidly, which made the daily average G peak at −34 W m^{-2} around 4 July, resulting in the lowest monthly mean values of G among the wintertime (see Table 3).

4.4. Seasonal Cycle of the Surface Energy Balance

Figure 7 shows the monthly mean variations in SEB components. On a yearly scale, $SR_{\downarrow}$ was the primary energy input, accounting for 50% of the incoming energy, while $LR_{\downarrow}$, SHF, and LHF accounted for 45%, 4%, and 1% of the incoming energy, respectively, through 2011. $LR_{\uparrow}$ dominated surface heat loss (58%), while the $SR_{\uparrow}$ and G contributed 40% and 2% (see Tables 2 and 3). During summertime, $SR_{\downarrow}$ and $LR_{\downarrow}$ dominate energy gains with 346 and 142 W m^{-2}. $SR_{\uparrow}$, $LR_{\uparrow}$, and G represent heat losses with seasonal average values of −287, −207, and −7 W m^{-2}, respectively. During the polar night, the main energy input and output terms

Table 3
Monthly Energy Balance Components and Surface Sublimation

		Sensible heat ($W\ m^{-2}$)	Latent heat ($W\ m^{-2}$)	Net shortwave radiation ($W\ m^{-2}$)	Net longwave radiation ($W\ m^{-2}$)	Ground flux ($W\ m^{-2}$)	Mass deposition ($kg\ m^{-2}$)
2011	Jan	10.8	3.3	47.1	−55.6	−5.5	3.1
	Feb	10.7	2.1	49.1	−63.0	1.1	1.8
	Mar	11.1	1.6	26.0	−37.6	−1.0	1.5
	Apr	14.0	1.4	3.6	−22.4	3.3	1.3
	May	6.0	1.2	0.0	−14.3	7.1	1.2
	Jun	7.4	1.0	0.0	−7.1	−1.3	0.9
	Jul	10.2	3.6	0.0	−8.1	−5.7	3.4
	Aug	9.1	2.4	0.7	−13.5	1.3	2.3
	Sep	17.1	1.9	20.7	−37.3	−2.4	1.7
	Oct	14.6	2.1	49.6	−52.1	−14.1	1.9
	Nov	27.0	3.2	71.3	−75.4	−26.0	2.9
	Dec	10.9	1.9	81.3	−77.3	−16.8	1.8
Average		12.4	2.1	29.1	−38.7	−5.0	2.0
						Total	23.8

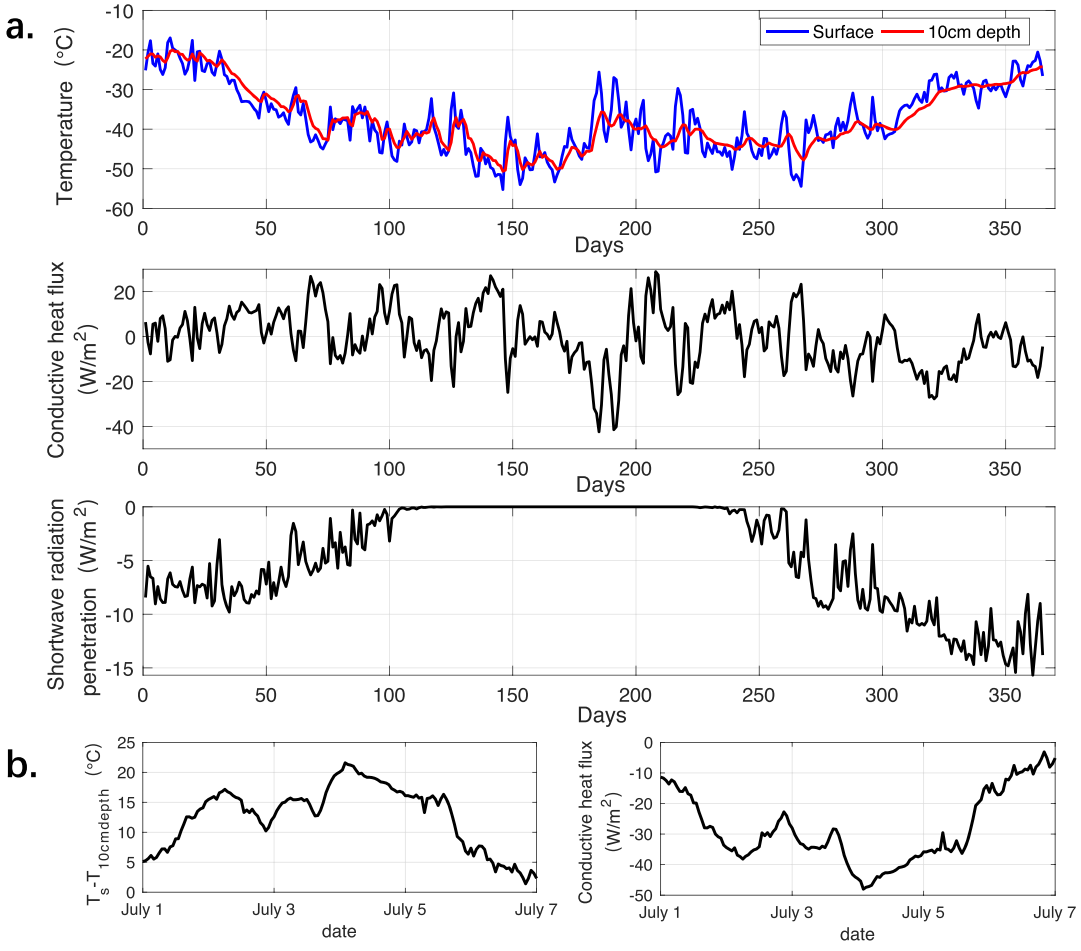

Figure 6. (a) Daily mean values of snow surface temperature, 40-cm snow temperature, conductive heat flux, and the shortwave radiation penetration. (b) Difference of snow temperature between snow surface and 10-cm depth, conductive heat flux during one intrusion event in July 2011 in hourly means.

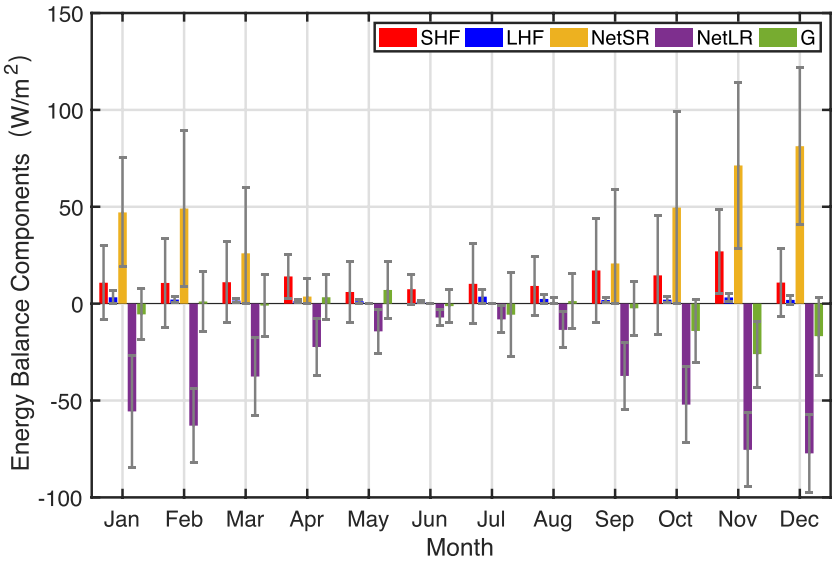

Figure 7. Monthly mean values of SEB components. (Different color bars are used to represent different SEB components. Red = sensible heat flux, blue = latent heat flux, yellow = net shortwave radiation, purple = net longwave radiation, green = conductive heat flux. Error bars are defined as the standard deviation.)

are $LR_{\downarrow}$ and $LR_{\uparrow}$, with seasonal average values of 149 and −159 W m^{-2}, respectively. The contributions of SHF and LHF increased, accounting for 6% and 1.4% of the incoming energy, respectively.

Ding et al. (2015) evaluated the surface mass balance along the CHINARE traverse and obtained an average mass accumulation rate in the latest decade near the Panda-1 Station could be nearly 39.3 kg · m^{-2} · a^{-1}. As deduced from LHF, the total amount of frost deposition in 2011 reached 23.8 kg · m^{-2} (Table 3), 61% of the total accumulation. The most intense deposition occurred in July, in conjunction with marine air intrusions. A similar frost deposition event occurred in January (Table 3). Although the humidity gradient was small from April to October, average LHF could still reach a value of 2 W m^{-2} under high wind speed conditions.

4.5. Diurnal Cycle of Energy Balance

Figure 8 shows the mean diurnal variation of temperature, snow surface temperature, and SEB components for different seasons. The daily cycle is most pronounced during summer and almost disappears in winter. On summer days, SRnet varies with the change in solar altitude angle, with a minimum at approximately 4:00 LT (local time, UTC +05:00) and reaching the peak at 16:00 LT every day. Conversely, SHF, LHF, and G generally decrease first and increase later in the day. These follow the strong response in surface temperature to the shortwave forcing, which made the surface temperature change faster than the air leading to convection/sublimation in early morning with a change in sign later in the day. The snow surface temperature cycle was approximately 3 hr ahead of the air temperature and started to exceed the air temperature at 10:00 LT, becoming lower again at approximately 18:00 LT because of the radiative cooling. During wintertime, the temperature gradient and therewith the fluxes remain essentially unchanged over the day. G follows subsurface temperature gradients and has different peaking times in different seasons. Similar lag results are also observed at Dome C and Halley Stations (King et al., 2006; Vignon, Hourdin, Genthon, et al., 2017). Net longwave radiation loss lags the net shortwave radiation by approximately one hour, which was similar to the results of the study by Van As, Van den Broeke, Reijmer et al. (2005).

5. Discussion

5.1. Comparison With Other Studies

The daily mean value of SRnet in summer at Panda-1 Station was 59 W m^{-2}, close to AWS measurements in the katabatic wind zone of DML (Van den Broeke, et al., 2004a). However, the albedo at Panda-1 was smaller (0.81 versus 0.84 annually); this difference may be attributed to the much larger accumulation in DML (244–313 mm w. e. a^{-1}; Van den Broeke et al., 2004b) than in the Panda-1 area (39 mm w. e. a^{-1}; Ding et al., 2015).

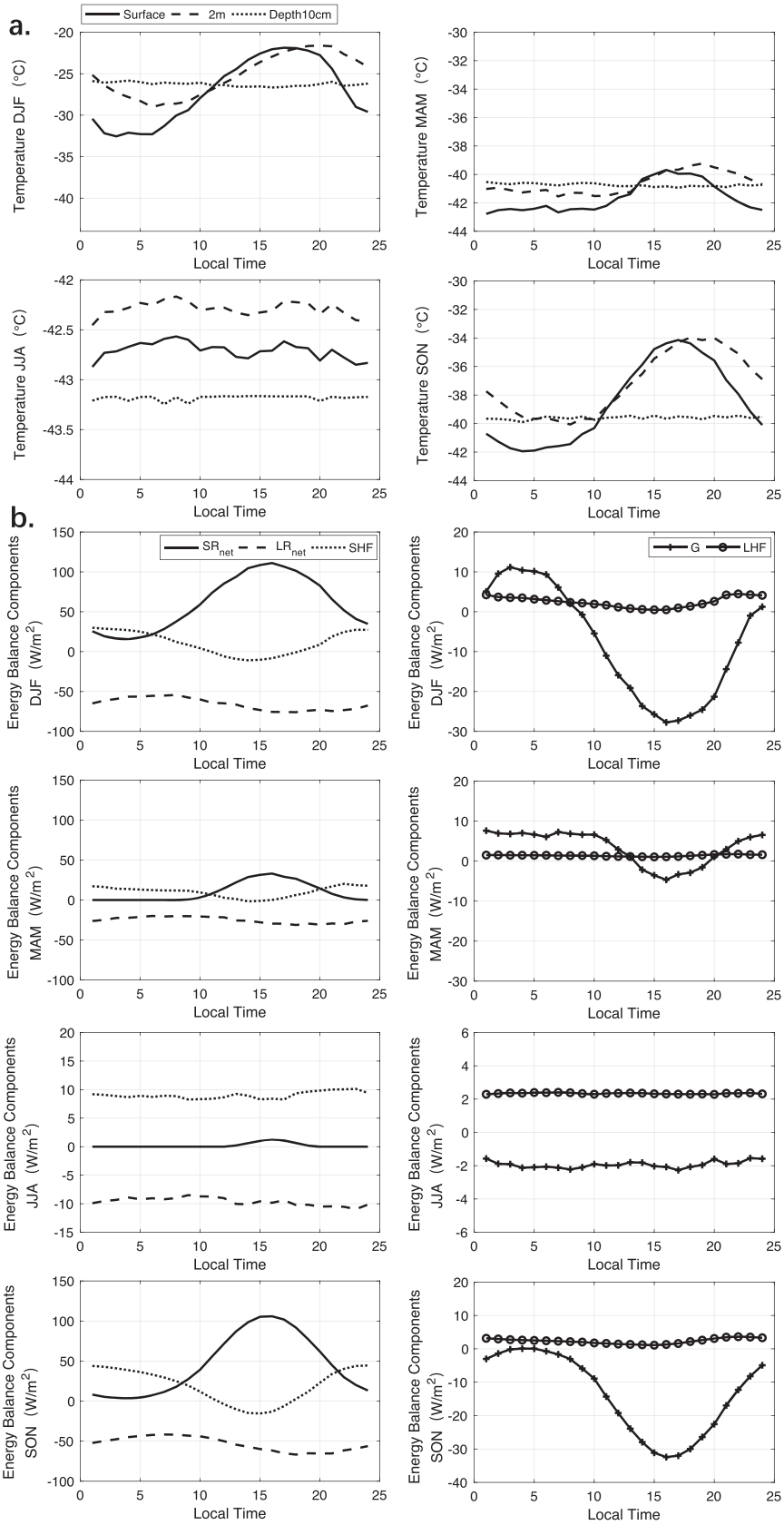

Figure 8. Mean diurnal curves of (a) daily air temperature, snow surface temperature, and (b) energy balance components in different seasons.

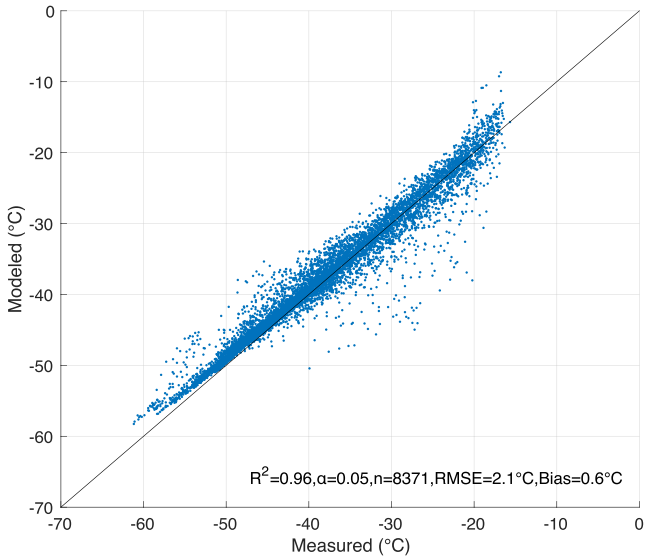

Figure 9. Measured versus modeled surface temperature at Panda-1 Station (RMSE = root mean square error).

At Panda-1, metamorphic grain growth is therefore stronger which reduces the albedo, leading to larger SRnet. The annual mean albedo at Mizuho Station, where accumulation is near-zero, could become be as low as 0.78 (Ohata et al., 1985). The annual average $LR_{\uparrow}$ at Panda-1 was 175 W m^{-2}, which is ~50 W m^{-2} smaller than the AWS 6 site in Van den Broeke, et al. (2004a) due to the lower surface temperature at Panda-1. LRnet at AWS6 in DML and Panda-1 AWS are similar in summer, while Panda-1 shows a smaller longwave energy loss in winter owing to more cloudy weather.

At Panda-1, the snow surface would always be colder than the low-level atmosphere, representing the temperature inversion near the surface and a positive SHF, similar to the findings at Zhongshan and Dome Argus Stations (Bian et al., 2013; Ding et al., 2015). The daily mean value of SHF at Panda-1 was 12 W m^{-2}. Although the average daily wind speeds of the two katabatic sites in DML (AWS 5 and 6) were smaller, the average SHF values were larger at 22 and 24 W m^{-2}, respectively (Van den Broeke et al., 2005). For the katabatic region in the central part of DML, Thiery et al. (2012) found average values of 33 W m^{-2}. These values are significantly larger than those in our study. We assign these differences to cloud cover, which may be larger at Panda-1, as well as potential inaccuracies in the reanalysis data sets and measured data in winter, with potential riming problems.

Synoptic weather systems have the potential to strongly impact the surface energy flux through longwave radiation and mixing (Gallée & Gorodetskaya, 2010; Brauna et al., 2001; Xie et al., 2002; Genthon et al., 2013; Bozkurt et al., 2018; Vignon et al., 2018). Bozkurt et al. (2018) studied a record-setting temperature event occurred at the northern tip of the Antarctica Peninsula (AP), caused by an atmospheric river that triggered a widespread foehn event. Cloud formation at the windward side provides the upper atmosphere with heat via water vapor condensation, also increasing the temperature at the leeward (foehn) side. Vignon et al. (2018) showed that deep, strong advection of lower latitude air toward Dome C caused high temperature and moisture anomalies at its western flank, rapidly increasing $LR_{\downarrow}$ and skin temperature. Interestingly at Panda-1, the major warm air intrusion increased not only the snow surface and air temperatures but also SHF and LHF to values in excess of 40 and 18 W m^{-2}. This finding suggests that a strong blocking in the upper air and a deep surface cyclone are key predictors for maritime air intrusions. Xie et al. (2002) discussed the formation and development of cyclones in Prydz Bay and calculated that SHF and LHF in the open water area could increase to 490 and 260 W m^{-2}, respectively. A significant gap remains between models and observations on these abrupt changes in Antarctica (Gallée & Gorodetskaya, 2010; Genthon et al., 2013; Vignon et al., 2018). Improving this requires additional observational data from the katabatic wind zone in the future, preferably using eddy-correlation and radiation sensors that can cope with the harsh climate conditions.

5.2. Uncertainty Evaluation

Only little snow accumulated at Panda-1 during 2011 (15.5 kg · m^2 · a^{-1}), and no melting occurred. When SEB components are calculated separately, using observed surface temperature from $LR_{\uparrow}$, we found a positive net energy residual. Instead, we assumed the SEB to be closed and used an iterative approach to find surface temperature, which has the added advantage that we can evaluate modeled T_s with observations (Thiery et al., 2012). Comparing modeled and measured T_s (Figure 9) yields average and root mean square errors of 0.6 and 2.1 °C, respectively, with an R^2 value of 0.96. These are reasonable results, given the data gap filling that was needed. The choice of stability function may have a strong impact on the flux calculation while the atmosphere is not close to neutrality. Using profiles measurements, Vignon, Genthon, et al. (2017) indicated that no pair of dimensionless gradients showed good agreement for both ϕ_m, ϕ_h at Dome C. Because at Panda-1 the atmosphere is close to neutral most of the time, we consider the impact of the choice of stability function to be small.

Table 4
Sensitivity Tests With Different Parameters

Parameters	△SHF	△LHF	△Conductive heat flux
Control	12.4 W/m^2	2.1 W/m^2	−0.5 W/m^2
$Z_{ov} = Z_{ot} = Z_{oq}$	−5.0%	+12.2%	+63.4%
$10Z_{ov}$	−3.2%	−4.6%	+86.9%
$Z_{ov}/10$	−3.2%	−4.6%	+86.9%
T_a + 1 °C	+10.4%	+1.2%	−232.5%
T_a − 1 °C	−16.9%	−8.9%	+403.1%
RH + 5%	−7.3%	+22.7%	+73.3%
RH − 5%	+0.9%	−31.8%	+100.5%
WS − 1.5 m/s	−5.9%	−26.2%	+226.4%
40 cm T_{snow}	−3.5%	−9.1%	+111.1%
Snow height variation (one year)	−3.2%	−4.3%	+85.9%
No shortwave penetration	−30.2%	−18.9%	−51.1%

We assessed the SEB uncertainty arising from the assumption of a non-changing sensor height, using the available snow stake record (Ding et al., 2011; Ding et al., 2015). We found that including the 10-year annual average snow surface height change of ~4 cm per year would lead to small changes of −3% and −4% in SHF and LHF, and about 0.5 W m^{-2} in G, respectively.

Subsequently, we tested for uncertainties related to radiation errors in the temperature measurements. For instance, Martin and Scherer (2001) showed that the offsets of naturally ventilated sensors could be 0.8 and 0.2 K at the height 1.1 and 5.2 m (Martin & Scherer, 2001; Matthias et al., 2008). We performed a number of sensitivity tests to quantify the uncertainties due to such measurement errors and other assumptions (see Table 4). SHF was mostly affected by the moisture and air temperature uncertainties, where variations of 5% RH and 1 °C air temperature invoked changes of 7% and 17%, respectively. LHF was more sensitive to the moisture and roughness length assumptions, where a 5% decrease in RH decreased LHF by 32%, while a 1 °C change in air temperature led to a variation of 8.9%. When assuming $z_{ov} = z_{ot} = z_{oq}$, LHF increased by 12.2%.

G is relatively sensitive to parameter perturbations due to its small magnitude. For instance, G doubled when the reanalysis data set errors on wind speed were also considered, but remained small in absolute sense. The uncertainty that arises from using wind speed from ERA5 was tested by applying a −1.5-m/s bias error, resulting in a −6% and −26% change in SHF and LHF, respectively.

We also assessed the combined effect of the uncertainties in the turbulence heat fluxes owing to uncertainties in relative humidity and temperature measurements (Figure 10). According to the method from Barral et al. (2014), we carried out a Monte Carlo test with 40 resamples whose starting error were ±2%, ±0.3 °C in relative humidity and temperature, respectively. It showed that the uncertainty in SHF and LHF were both amplified

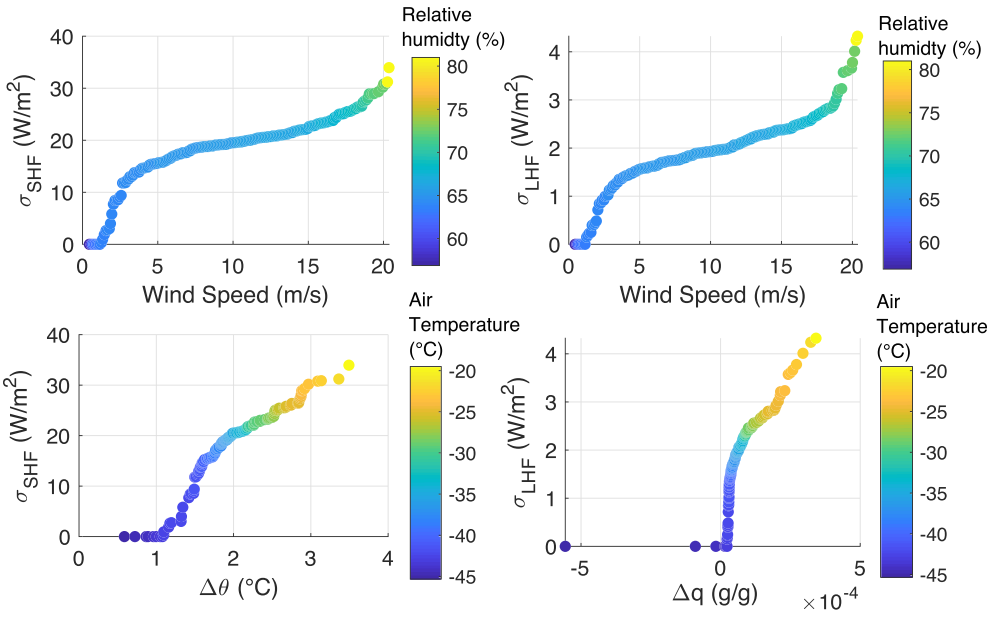

Figure 10. (top) Estimation of uncertainty into sensible and latent heat flux calculation using bulk method versus wind speed with an error of ±2% for relative humidity. (bottom) Estimation of uncertainty into sensible and latent heat flux calculation using bulk method versus temperature and specific humidity differences between 2 m and surface with an error of ±0.3 °C for temperature. σ=standard deviation.

as the wind speed increased which could be explained by the wind scale u_* in equations (4) and (5). High wind speed also could lead the strong mixing and lower temperature, humidity gradients (Barral et al., 2014) which mean to made the 2-m relative humidity close to the snow surface. However, the relationship between σ_{SHF} and the difference of potential temperature, σ_{LHF}, and the difference of specific humidity (between 2 m and snow surface) indicated that the mixing effect on decreasing surface atmosphere gradients may has some limit. Comparing to uncertainties assessment via profile calculations in the Barral et al. (2014), the SEB closure in this paper made better measurement uncertainties which was similar to the performance of Crocus model (Barral et al., 2014). On the whole, this model is suitable for our SEB calculation.

We do not consider uncertainties in assumed snow density to play a major role; the snow densities at our site (10 cm: 381 kg m^3, 40 cm: 446 kg m^3; measured in December 2012) were very close to Panda-N Station (10 cm: 373 kg m^3, 40 cm: 448 kg m^3; measured in January 2011) which is ~100 km away. This implies that the physical properties of the surface snow are homogeneous in the wind glazed area. Precipitation and drifting snow sublimation were not considered in our calculations because of a lack of measurements. At Dome A, Ding et al. (2016) found a mass accumulation rate of 23 kg $\cdot$ m^{-2} $\cdot$ a^{-1}, and surface sublimation of 2.2 kg $\cdot$ m^{-2} $\cdot$ a^{-1}. The annual average wind speed at Panda-1 Station is close to 10.5 m s^{-1}, whereas at Dome A Station it is less than 3 m s^{-1}. The sublimation of drifting snow at Panda-1 may thus be much larger than those at Dome A Station. Van den Broeke, et al. (2004b) noted that the column drifting snow sublimation could reach nearly 120 mm w.e. over four years in the katabatic wind zone of DML. Panda-1 Station has a higher wind speed in winter, potentially resulting in more drifting snow sublimation, which may thus be a key source to improve the performance of the SEB model in the study area. Due to the lack of snow micromeasurements, detailed estimation of drifting snow sublimation has not been carried out.

6. Conclusion

We calculated the SEB using data of Panda-1 AWS, located in the katabatic wind area in Princess Elizabeth Land, East Antarctica. In this katabatic wind zone, $SR_\downarrow$ and $LR_\downarrow$ were the main energy sources during summer, with seasonal average values of 346 and 142 W m^{-2}. SHF, LHF, and G added 11, 2, and 6 W m^{-2}. $SR_\uparrow$, $LR_\uparrow$, and shortwave radiation penetration were the energy sinks with seasonal average values of −287, −207, and −9 W m^{-2}, respectively. In winter, the main energy input and output terms of SEB were $LR_\downarrow$ and $LR_\uparrow$ with seasonal average values of 149 and −159 W m^{-2}, respectively. A significant daily cycle in SEB components is found in summer. Because of the different thermal properties of snow and air, SHF and LHF showed diurnal variations opposite to the solar forcing. Longwave energy loss mainly followed snow surface temperature.

We also analyzed the impact on the SEB at Panda-1 site of two maritime air intrusions from blocked southern Indian Ocean cyclones. The blocking was caused by the southward extension of the Indian Ocean subtropical high in the upper atmosphere near Prydz Bay. As a result, the cyclone stagnated and strengthened in situ. The northerly circulation at the front of the cyclone caused maritime air masses to reach Panda-1 Station, rapidly increasing LRnet, SHF, and LHF and decreasing G, with increases in excess of 25 W m^{-2}.

The annual surface frost deposition at Panda-1 was 23.8 kg m^{-2} in 2011, which accounts for 61% of the 10-year annual average net accumulation.

This study provides important new understanding on the interaction between ice/snow and atmosphere in the katabatic wind zone in this understudied part of East Antarctica. More long-term observations and notably short-term eddy covariance experiments from this region are urgently needed to further improve weather and climate model performance in Antarctica.

Acknowledgments
This research is supported by the Natural Science Foundation of China (41771064), the National Basic Research Program of China (2016YFC1400303), and the Basic Fund of the Chinese Academy of Meteorological Sciences (2018Z001). As for the data availability, ERA5 reanalysis data sets are freely distributed on the Climate Date Store (https://cds.climate.copernicus.eu/cdsapp#!/search?type=dataset). Meteorological data are made available on the website of PANGAEA (Data Publisher for Earth & Environmental Science). The direct link is https://doi.pangaea.de/10.1594/PANGAEA.905761. The authors thank the support from Institude of Tibetan Plateau and Polar Meteorology. Besides, we also deeply appreciate the staffs for their hard work on the Panda-1 Station under the inland Antarctica condition and the comments from two anonymous referees.

References

Andersen, T. K., Radcliffe, D. E., & Shepherd, J. M. (2013). Quantifying surface energy fluxes in the vicinity of inland-tracking tropical cyclones. *Journal of Applied Meteorology & Climatology*, *52*(12), 2797–2808.

Andreas, E. L. (1987). A theory for the scalar roughness and the scalar transfer coefficients over snow and sea ice. *Boundary-Layer Meteorology*, *38*(1-2), 159–184.

Argentini, S., Pietroni, I., Mastrantonio, G., Viola, A. P., Dargaud, G., & Petenko, I (2014). Observations of near surface wind speed, temperature and radiative budget at Dome C, Antarctic Plateau during 2005. *Antarctic Science*, *26*, 104–112.

Barral, H., Genthon, C., Trouvilliez, A., et al. (2014). Blowing snow at D17, Adélie Land, Antarctica: Atmospheric moisture issues. *Cryosphere Discussions*, *8*(3), 2759–2798.

Beljaars, A. C. M., & Holtslag, A. A. M. (1991). Flux parameterization over land surfaces for atmospheric models. *Journal of Applied Meteorology*, *30*(3), 327–341.
Berdahl, P., & Fromberg, R. (1981). An empirical method for estimating the thermal radiation of clear skies. *Solar Energy. Report Number*, LBL-12720.
Bian, L., Lu, L., & Pengqun, J. (1991). Observational study of radiation balance components over Laresman hills. *Antarctic Research*, *3*(4), 43–51.
Bian, L., & Zhong, et al. (2013). Structure and seasonal changes in atmospheric boundary layer on coast of the east Antarctic continent. *Advances in Polar Science*, *24*(3), 139–146.
Bintanja, R. (2001). Snowdrift sublimation in a katabatic wind region of the Antarctic Ice Sheet. *Journal of Applied Meteorology*, *40*(11), 1952–1966.
Bintanja, R., & Reijmer, C. H. (2001). A simple parameterization for snowdrift sublimation over Antarctic snow surfaces. *Journal of Geophysical Research Atmospheres*, *106*(D23), 31,739–31,748.
Bintanja, R., & Van den Broeke, M. R. (1995). The surface energy balance of Antarctic snow and blue ice. *Journal of Applied Meteorology*, *34*(4), 902–926.
Bliss, A. K., Cuffey, K. M., & Kavanaugh, J. L. (2011). Sublimation and surface energy balance of Taylor Glacier, Antarctica. *Journal of Glaciology*, *57*(204), 684–696.
Bolton, D. (1980). The computation of equivalent potential temperature. *Monthly Weather Review*, *108*, 1046–1953.
Bozkurt, D., Rondanelli, R., Marin, J. C., & Garreaud, R. (2018). Foehn event triggered by an atmospheric river underlies record-setting temperature along continental Antarctica. *Journal of Geophysical Research: Atmospheres*, *123*, 3871–3892.
Braun, M., Saurer, H., Vogt, S., Simões, J. C., & Goßmann, H. (2001). The influence of large-scale atmospheric circulation on the surface energy balance of the King George Island ice cap. *International Journal of Climatology*, *21*, 21–36.
Brun, E., Six, D., Picard, G., et al. (2012). Snow/atmosphere coupled simulation at Dome C, Antarctica. *J Glaciol*, *52*, 721–726.
Carroll, J. J. (1982). Long-term means and short-term variability of the surface energy balance components at the south pole. *Journal of Geophysical Research Oceans*, *87*(C6), 4277–4286.
Chen, Z., Lingen, B., Cunde, X., et al. (2007). Seasonal variations of the near surface layer parameters over the Antarctic ice sheet in Princess Elizabeth Land, East Antarctica. *Chinese Journal of Polar Science*, *18*(2), 122–134.
Ding, M., Xiao, C., Li, Y., et al. (2011). Spatial variability of surface mass balance along a traverse route from Zhongshan station to Dome A, Antarctica. *Journal of Glaciology*, *57*(204), 658–666.
Ding, M., Xiao, C., Yang, Y., et al. (2016). Re-assessment of recent (2008–2013) surface mass balance over Dome Argus, Antarctica. *Polar Research*, *35*(2016).
Ding, M., Xiao, C., Zhang, R., et al. (2017). Snowdrift effect on snow deposition: Insights from a comparison of a snow pit profile and meteorological observations ineast Antarctica. *Science China Earth Sciences*, *60*(4), 672–685.
Ding, M. H., Xiao, C. D., Chuanjin, L. I., et al. (2015). Surface mass balance and its climate significance from the coast to Dome A, East Antarctica. *Science China Earth Sciences*, *58*(10), 1787–1797.
Dyer, A. J. (1974). A review of flux-profile relationships. *Boundary-Layer Meteorology*, *7*(3), 363–372.
Eisen, O., Frezzotti, M., Genthon, C., et al. (2009). Ground-based measurements of spatial and temporal variability of snow accumulation in East Antarctica. *Reviews of Geophysics*, *46*(2), RG2001-1–RG2001-39.
Frezzotti, M., Gandolfi, S., & Urbini, S. (2002). Snow megadunes in Antarctica: Sedimentary structure and genesis. *Journal of Geophysical Research Atmospheres*, *107*(D18), ACL-1-ACL 1-12.
Fu, L., Lingen, B., Cunde, X., Changgui, L., & Minghu, D. (2015). An observational study of the radiation balance on eastern Antarctic Plateau. *Acta Meteorologica Sinica*, *73*(1), 211–219.
Fujita, K. (2000). Effect of summer accumulation on glacier mass balance on the Tibetan Plateau revealed by mass-balance model. *Journal of Glaciology*, *46*(153), 244–252.
Gallée, H., & Gorodetskaya, I. (2010). Validation of a limited area model over Dome C, Antarctic Plateau, during winter. *Climate Dynamics*, *23*, 61–72.
Gallée, H., Guyomarc'H, G., & Brun, E. (2001). Impact of snow drift on the Antarctic ice sheet surface mass balance: Possible sensitivity to snow-surface properties. *Boundary-Layer Meteorology*, *99*(1), 1–19.
Genthon, C., Six, D., Galléee, H., Grigioni, P., & Pellegrini, A. (2013). Two years of atmospheric boundary layer observations on a 45m tower at Dome C on the Antarctic Plateau. *Journal of Geophysical Research: Atmospheres*, *118*, 3218–3232.
Gubler, S., Gruber, S., & Purves, R. S. (2012). Uncertainties of parameterized surface downward clear-sky shortwave and all-sky longwave radiation. *Atmospheric Chemistry and Physics*, *12*(11), 5077–5098.
Heil, P., Ian, A., et al. (1996). Seasonal and interannual variations of the oceanic heat flux under a landfast antarctic sea ice cover. *Journal of Geophysical Research Oceans*, *101*(C11), 25,741–25,752.
Huang W. R. (2008). Interannual and intraseasonal variations of the energy balance over the polar regions and its climatic implications. Dissertations & Theses - Gradworks.
Huybrechts, P. (1990). A 3-D model for the Antarctic ice sheet: A sensitivity study on the glacial-interglacial contrast. *ClimDyn*, *5*(2), 79–92.
Iqbal, M. (1983). *An introduction to solar radiation*. Toronto, Canada: Academic Press.
King, J. C., Anderson, P. S., Smith, M. C., et al. (1996). The surface energy and mass balance at Halley, Antartica during winter. *Journal of Geophysical Research Atmospheres*, *101*(D14), 19,119–19,128.
King, J. C., Argentini, S. A., & Anderson, P. S. (2006). Contrasts between the summertime surface energy balance and boundary layer structure at Dome C and Halley stations, Antarctica. *J. Geophys. Res.*, *111*, D02105. https://doi.org/10.1029/2005JD006130
King, J. C., Kirchgaessner, A., Bevan, S., et al. (2017). The impact of fohn winds on surface energy balance during the 2010–11 melt season over Larsen C Ice Shelf, Antarctica. *Journal of Geophysical Research: Atmospheres*.
Kuhn, M., Kundla, L. S., & Stroschein, L. A. (1977). The radiation budget at Plateau Station, Antarctica, 1966–1967. Meteorological Studies at Plateau Station, Antarctica. *American Geophysical Union*, 41–73.
Kumar, L., Skidmore, A. K., & Knowles, E. (1997). Modelling topographic variation in solar radiation in a gis environment. *International Journal of Geographical Information Science*, *11*(5), 475–497.
Lei, R., Li, N., Heil, P., Cheng, B., Zhang, Z., & Sun, B. (2014). Multiyear sea ice thermal regimes and oceanic heat flux derived from an ice mass balance buoy in the arctic ocean. *Journal of Geophysical Research: Oceans*, *119*(1), 537–547.
Lei, R., Li, Z., Cheng, B., Zhang, Z., & Heil, P. (2010). Annual cycle of landfast sea ice in Prydz Bay, east Antarctica. *J. Geophys. Res.*, *115*, C02006.

Liston, G. E., Jan-Gunnar, W., Oddbjā, R. B., et al. (1999). Below-surface ice melt on the coastal Antarctic ice sheet. *Journal of Glaciology*, *45*(150), 273–285.

Marsiat, I., & Bamber, J. L. (1997). The climate of antarctica in the UGAMP GCM: Sensitivity to topography. *Annals of Glaciology*, *25*(25), 79–84.

Martin, A., & Scherer, D. (2001). A physically based method for correcting temperature data measured by naturally ventilated sensors over snow. *Journal of Glaciology*, *47*(159), 665–670.

Mastrantonio, G., Malvestuto, V., Argentini, S., et al. (1999). Evidence of a convective boundary layer developing on the Antarctic Plateau during the summer. *Meteorology & Atmospheric Physics*, *71*(1-2), 127–132.

Matthias, M., Desjardins, R. L., Gao, Z., & Van Haarlem, R. (2008). Errors of naturally ventilated air temperature measurements in a spatial observation network. *Journal of Atmospheric and Oceanic Technology*, *25*(11), 2145–2151.

Ohata, T., Kobayashi, S., Ishikawa, N., & Kawaguchi, S. (1985). Heat balance at the snow surface in a katabatic wind zone, East Antarctica. *Ann. Glaciol.*, *6*, 174–177.

Qin, T., Lixin, W., & Cheng, L. (2017). The statistic and variance of cyclones enter in scientific investigation station of China in Antarctic. *Acta Oceanologica Sinica*, *39*(5), 44–60.

Randall, D. A., Cess, R. D., Blanchet, J. P., et al. (1992). Intercomparison and interpretation of surface energy fluxes in atmospheric general circulation Models. *J.geophy.res*, *97*(20), 3711–3724.

Rinke, A., Ma, Y., Bian, L., Xin, Y., Dethloff, K., Persson, P. O. G, et al. (2012). Evaluation of atmospheric boundary layer–surface process relationships in a regional climate model along an East Antarctic traverse. *J. Geophys. Res.*, *117*, D09121.

Rinke, A., Maturilli, M., Graham, R. M., Matthes, H., & Moore, J. C. (2017). Extreme cyclone events in the arctic: wintertime variability and trends. *Environmental Research Letters*, *12*(9), 094006.

Scambos, T. A., Frezzotti, M., Haran, T., et al. (2012). Extent of low-accumulation "wind glaze" areas on the East Antarctic plateau: Implications for continental ice mass balance. *Journal of Glaciology*, *58*(210), 633–647.

Simmonds, I., & Keay, K. (2000). Mean southern hemisphere extratropical cyclone behavior in the 40-year NCEP–NCAR reanalysis. *Journal of Climate*, *13*(5), 873–885.

Sturm, M., Holmgren, J., König, M., et al. (1997). The thermal conductivity of seasonal snow. *Journal of Glaciology*, *43*(143), 26–41.

Sturm, M., Perovich, D. K., & Holmgren, J. (2002). Thermal conductivity and heat transfer through the snow on the ice of the Beaufort Sea. *J. Geophys. Res.*, *107*(C10), 8043.

Sun, W., Qin, X., Wang, Y., Yang, X. G., Zhang, T., & Liu, Y. S. (2018). The response of surface mass and energy balance of a continental glacier to climate variability, western Qilian Mountains, China. *Climate Dynamics*, *50*(9-10), 3557–3570.

Sun, W. J., Qin, X., Ren, J. W., Yang, X. G., Zhang, T., & Liu, Y. S. (2012). The surface energy budget in the accumulation zone of the laohugou glacier no. 12 in the western Qilian Mountains, China, in summer 2009. *Arctic Antarctic & Alpine Research*, *44*(3), 296–305. https://doi.org/10.1657/1938-4246-44.3.296

Thiery, W., Gorodetskaya, I. V., Bintanja, R., et al. (2012). Surface and snowdrift sublimation at Princess Elisabeth station, East Antarctica. *Cryosphere*, *6*(4), 841–857.

Town, M. S., & Walden, V. P. (2009). Surface energy budget over the south pole and turbulent heat fluxes as a function of an empirical bulk Richardson number. *J Geophys Res*, *114*, D22107.

Van As, D., Van den Broeke, M. R., Reijmer, C., et al. (2005). The summer surface energy balance of the high Antarctic plateau. *Boundary-Layer Meteorology*, *115*(2), 289–317.

Van As, D., Van den Broeke, M. R., & Roderik, V. D. W. (2005). Daily cycle of the surface layer and energy balance on the high Antarctic Plateau. *Antarctic Science*, *17*(1), 121–133.

Van den Broeke, M. R., Reijmer, C., Van As, D., et al. (2006). Daily cycle of the surface energy balance in Antarctica and the influence of clouds. *International Journal of Climatology*, *26*(12), 1587–1605.

Van den Broeke, M. R., Reijmer, C., & van de Wal, R. (2004a). Surface radiation balance in Antarctica as measured with automatic weather stations. *J. Geophys. Res.*, *109*, D09103.

Van den Broeke, M. R., Reijmer, C. H., van As, D., van de Wal, R. S. W., & Oerlemans, J. (2005). Seasonal cycles of Antarctic surface energy balance from Automatic Weather Stations. *Annals of Glaciology*, *41*, 131–139.

Van den Broeke, M. R., Reijmer, C. H., Van De Wal, R. S. W. (2004b). A study of the surface mass balance in Dronning Maud Land, Antarctica, using automatic weather stations. *Journal of Glaciology*, *50*(171), 565–582.

Van den Broeke, M. R., Van As, D., Reijmer, C., et al. (2003). Assessing and improving the quality of unattended radiation observations in Antarctica. *Journal of Atmospheric & Oceanic Technology*, *21*(9), 1417–1431.

Van den Broeke, M. R., Van As, D., Reijmer, C., et al. (2005). Sensible heat exchange at the Antarctic snow surface: A study with automatic weather stations. *International Journal of Climatology*, *25*(8), 1081–1101.

Vignon, E., Genthon, C., Barral, H., Amory, C., et al. (2017). *Momentum- and parametrization at Dome C*. Antarctica: A sensitivity study. Boundary-Layer Meteorology.

Vignon, E., Hourdin, F., Genthon, C., Gallée, H., Bazile, E, Lefebvre, M. P. et al. (2017). Antarctic boundary layer parametrization in a general circulation model: 1D simulations facing summer observations at Dome C. *Journal of Geophysical Research: Atmospheres*, *122*, 6818–6843.

Vignon, E., Hourdin, F., Genthon, C., Van de Wiel, B. J. H., Gallée, H., et al. (2018). Modeling the dynamics of the atmospheric boundary layer over the Antarctic Plateau with a general circulation model. *Journal of Advances in Modeling Earth Systems*, *10*.

Wang, Y., Sodemann, H., Hou, S., et al. (2013). Snow accumulation and its moisture origin over Dome Argus, Antarctica. *Climate Dynamics*, *40*(3-4), 731–742.

Woods, C., Caballero, R., & Svensson, G. (2013). Large-scale circulation associated with moisture intrusions into the Arctic during winter. *Geophysical Research Letters*, *40*(17), 4717–4721.

Xie, S., Shan, M., Kewei, L., et al. (2002). Cyclone formation and development in the Antarctic Prydz Bay. *Acta Oceanologica Sinica*, *21*(1), 45–54.

Yang, D., Minghu, D., et al. (2018). Performance evaluation of FS-J1 four-component radiometer in Arctic environment. *Meteorological Science And Technology*, *46*(5), 845–854. https://doi.org/10.19517/j.1671-6345.20170586